Effect of porous surfaces on compressible boundary layers perturbed by free-stream disturbances

Pierre Ricco
UNIVERSITY OF SHEFFIELD, DEPARTMENT OF PSYCHOLOGY

01/04/2019
Final Report

REPORT DOCUMENTATION PAGE		*Form Approved* *OMB No. 0704-0188*

The public reporting burden for this collection of information is estimated to average 1 hour per response, including the time for reviewing instructions, searching existing data sources, gathering and maintaining the data needed, and completing and reviewing the collection of information. Send comments regarding this burden estimate or any other aspect of this collection of information, including suggestions for reducing the burden, to Department of Defense, Executive Services, Directorate (0704-0188). Respondents should be aware that notwithstanding any other provision of law, no person shall be subject to any penalty for failing to comply with a collection of information if it does not display a currently valid OMB control number.
PLEASE DO NOT RETURN YOUR FORM TO THE ABOVE ORGANIZATION.

1. REPORT DATE *(DD-MM-YYYY)* 08-02-2019	**2. REPORT TYPE** Final	**3. DATES COVERED** *(From - To)* 30 Sep 2015 to 29 Sep 2018	
4. TITLE AND SUBTITLE Effect of porous surfaces on compressible boundary layers perturbed by free-stream disturbances		**5a. CONTRACT NUMBER**	
		5b. GRANT NUMBER FA9550-15-1-0248	
		5c. PROGRAM ELEMENT NUMBER 61102F	
6. AUTHOR(S) Pierre Ricco		**5d. PROJECT NUMBER**	
		5e. TASK NUMBER	
		5f. WORK UNIT NUMBER	
7. PERFORMING ORGANIZATION NAME(S) AND ADDRESS(ES) UNIVERSITY OF SHEFFIELD, DEPARTMENT OF PSYCHOLOGY WESTERN BANK SHEFFIELD, S10 2TN GB		**8. PERFORMING ORGANIZATION REPORT NUMBER**	
9. SPONSORING/MONITORING AGENCY NAME(S) AND ADDRESS(ES) EOARD Unit 4515 APO AE 09421-4515		**10. SPONSOR/MONITOR'S ACRONYM(S)** AFRL/AFOSR IOE	
		11. SPONSOR/MONITOR'S REPORT NUMBER(S) AFRL-AFOSR-UK-TR-2019-0010	

12. DISTRIBUTION/AVAILABILITY STATEMENT
A DISTRIBUTION UNLIMITED: PB Public Release

13. SUPPLEMENTARY NOTES

14. ABSTRACT
Compressible pre-transitional boundary layers over flat and streamwise concave walls an exposed to free-stream vortical disturbances have been studied numerically and by asymptotic methods. Receptivity mechanisms have been explained for the first time, such as the generation and growth of nonlinear unsteady Gortler vortices, linear unsteady compressible Gortler vortices exposed to free-stream gusts, very first rigourous neutral curves of the incompressible Gortler vortices, and the competing effects of acoustic and vortical eigenmodes excited by free-stream disturbances. The output in terms of archival publications has been very good, i.e., six papers (+ one in revised submission in J. Fluid Mechanics), including three J. Fluid Mech. and one Phys. Fluids.

15. SUBJECT TERMS
EOARD, Porous wall

16. SECURITY CLASSIFICATION OF:			**17. LIMITATION OF ABSTRACT**	**18. NUMBER OF PAGES**	**19a. NAME OF RESPONSIBLE PERSON** SMITH, DOUGLAS
a. REPORT Unclassified	**b. ABSTRACT** Unclassified	**c. THIS PAGE** Unclassified	SAR		**19b. TELEPHONE NUMBER** *(Include area code)* 314-235-6013

Standard Form 298 (Rev. 8/98)
Prescribed by ANSI Std. Z39.18

Effect of Porous Surfaces on Compressible Boundary Layers Perturbed by Free-Stream Disturbances

THE UNIVERSITY OF SHEFFIELD

DEPARTMENT OF MECHANICAL ENGINEERING

Klebanoff modes and Görtler vortices in compressible boundary layers subject to free-stream vortical disturbances

Ph.D. student and post-doc researchers:
Samuele VIARO
Dr Eva ZINCONE
Dr Claudia ALVARENGA

Supervisor:
Dr. Pierre RICCO

December 17, 2018

The University Of Sheffield.

1 Presentations, conferences and archival journal papers

The research results have been presented at the following conferences and meetings:

- AFSOR hypersonic portfolio review, BICC, Arlington, Virginia, July 2018,
- AFSOR hypersonic portfolio review, NASA Langley, July 2017,
- AFSOR hypersonic portfolio review, BICC, Arlington, Virginia, July 2016,
- 2018 Ricco, P. Goldstein, M.E. Leading edge receptivity of a supersonic boundary layer to free-stream acoustic and vortical disturbances *Proc. 12th Euromech Fluid Mech. Conf., Vienna, Austria, 9th-13th Sept.*.

- 2018 Viaro, S. Ricco, P. Neutral stability curves of unsteady Görtler instability *Proc. 12th Euromech Fluid Mech. Conf., Vienna, Austria, 9th-13th Sept.*.

- 2017 Viaro, S. Ricco, P. Linear evolution of compressible Görtler instability triggered by free-stream vortical disturbances, 70th *Ann. Meeting APS Div. Fluid Dyn., Denver, 19th-21st Nov.*

- 2017 Ricco, P. Marensi, E. Wu, X. Nonlinear growth of unsteady streaks caused by free-stream vorticity in a compressible boundary layer, 70th *Ann. Meeting APS Div. Fluid Dyn., Denver, 19th-21st Nov.*

- 2017 Viaro, S. Ricco, P. Linear evolution of compressible Görtler instability triggered by free-stream vortical disturbances, *591 Euromech Colloquium "3-D Instability Mechanisms in Transitional and Turbulent flows", Bari, 18th-20th Sept.*

- 2017 Viaro, S. Ricco, P. Compressible Görtler vortices excited by free-stream vortical disturbances, 16th *Euromech European Turbulence Conf., Stockholm, 21st-24th August.*

- 2017 Marensi, E. Ricco, P. Wu, X. Nonlinear evolution of unsteady streaks in a compressible boundary layer subject to free-stream vorticity, *British Applied Mathematics Colloquium, Univ. Surrey, 10th-12th April.*

- 2017 Viaro, S. Ricco, P. Linear evolution of compressible Görtler vortices subject to free-stream vortical disturbance, *Proc. ICFM 2017: 19th Int. Conf. Fluid Mechanics, Prague, Czech Republic, 23rd-24th March.*

and published in the following journal papers:

- 2019 Viaro, S. Ricco, P. Compressible unsteady Görtler vortices subject to free-stream vortical disturbances ***Submitted (second revised submission) to J. Fluid Mech.***

- 2019 Goldstein, M.E. Ricco, P. Leading edge receptivity at subsonic and moderately supersonic Mach numbers ***Accepted in IntechOpen***

- 2018 Viaro, S. Ricco, P. Neutral stability curves of low-frequency Görtler flow generated by free-stream vortical disturbances, ***J. Fluid Mech. (Rapids)***, **845**, R1.

- 2018 Goldstein, M.E. Ricco, P. Non-localized instabilities resulting from leading-edge receptivity at moderate supersonic Mach numbers ***J. Fluid Mech.***, **838**, pp. 435-477.

- 2017 Marensi, E. Ricco, P. Growth and wall-transpiration control of nonlinear unsteady Görtler vortices forced by free-stream vortical disturbances ***Phys. Fluids***, **29**, 114106.

- 2017 Marensi, E. Ricco, P. Wu, X. Nonlinear unsteady streaks engendered by the interaction of free-stream vorticity with a compressible boundary layer ***J. Fluid Mech.***, **817**, pp. 80-121.

- 2016 Ricco, P. Walsh, E.J. Brighenti, F. McEligot, D.M. Growth of boundary-layer streaks due to free-stream turbulence ***Int. J. Heat Fluid Flow***, **61**, pp. 272-283.

1

2   Introduction

The perturbations triggered by free-stream vortical disturbances in compressible boundary layers developing over concave walls are studied numerically and through asymptotic methods. We employ an asymptotic framework based on the limit of high Görtler number, the scaled parameter defining the centrifugal effects, we use an eigenvalue formulation where the free-stream forcing is neglected, and solve the receptivity problem by integrating the compressible boundary-region equations complemented by appropriate initial and boundary conditions which synthesize the influence of the free-stream vortical flow. Near the leading edge, the boundary-layer perturbations develop as thermal Klebanoff modes and, when centrifugal effects become influential, these modes turn into thermal Görtler vortices, i.e., streamwise rolls characterized by intense velocity and temperature perturbations. The high-Görtler-number asymptotic analysis reveals the condition for which the Görtler vortices start to grow. The Mach number is destabilizing when the spanwise diffusion is negligible and stabilizing when the boundary-layer thickness is comparable with the spanwise wavelength of the vortices. When the Görtler number is large, the theoretical analysis also shows that the vortices move towards the wall as the Mach number increases. These results are confirmed by the receptivity analysis, which additionally clarifies that the temperature perturbations respond to this reversed behavior further downstream than the velocity perturbations. A matched-asymptotic composite profile, found by combining the inviscid core solution and the near-wall viscous solution, agrees well with the receptivity profile sufficiently downstream and at high Görtler number. The Görtler vortices tend to move towards the boundary-layer core when the flow is more stable, i.e., as the frequency or the Mach number increase, or when the curvature decreases. As a consequence, a region of unperturbed flow is generated near the wall. We also find that the streamwise length scale of the boundary-layer perturbations is always smaller than the free-stream streamwise wavelength. During the initial development of the vortices, only the receptivity calculations are accurate. At streamwise locations where the free-stream disturbances have fully decayed, the growth rate and wavelength are computed accurately by the eigenvalue analysis, although the correct amplitude of the Görtler vortices can only be determined by the receptivity calculations. It is further proved that the eigenvalue predictions of the growth rate and wavenumber worsen as the Mach number increases, as these quantities show a dependence on the wall-normal direction.

The neutral curves of the boundary-layer Görtler-vortex flow generated by free-stream disturbances, i.e., curves that distinguish the perturbation flow conditions of growth and decay, are computed through a receptivity study for different Görtler numbers, wavelengths, and low frequencies of the free-stream disturbance. The perturbations are defined as Klebanoff modes or strong and weak Görtler vortices, depending on their growth rate. The critical Görtler number below which the inviscid instability due to the curvature never occurs is obtained and the conditions for which only Klebanoff modes exist are thus revealed.

3   Scaling and equations of motion

We consider a uniform compressible air flow of velocity U_∞^* and temperature T_∞^* past a slightly concave plate with constant radius of curvature r^*. Hereinafter the asterisk $*$ identifies dimensional quantities. In the proximity of the surface, the flow is described by the orthogonal curvilinear coordinate system $\mathbf{x} = \{x, y, z\}$ that defines the streamwise, wall-normal, and spanwise directions. The conversion from the Cartesian to the curvilinear coordinates system is achieved through the Lamé coefficients $h_x = 1 - y^*/r^*, h_y = 1$, and $h_z = 1$ (Wu et al., 2011). The flow domain is represented in figure 1.

Small-intensity free-stream vortical perturbations are passively advected by the uniform free-stream flow and are modeled as three-dimensional vortical disturbances of the gust type, which,
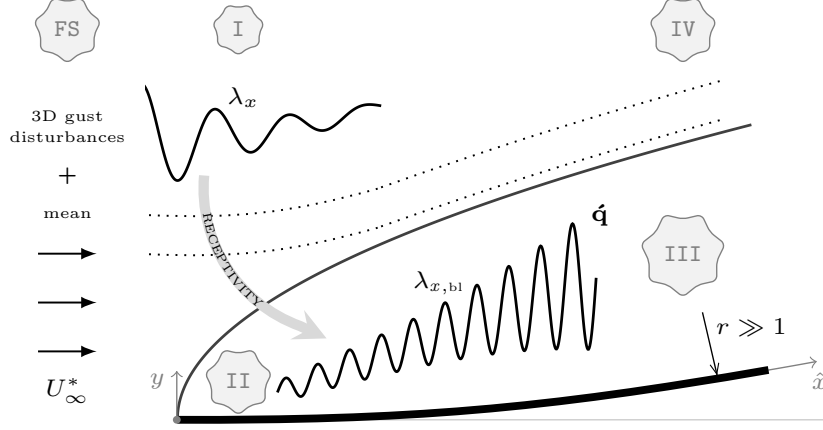
2

Figure 1: Schematic of the boundary-layer asymptotic regions $\mathtt{I}, \mathtt{II}, \mathtt{III}, \mathtt{IV}, \mathtt{FS}$ and the receptivity mechanism to free-stream vortical disturbances, where λ_x is the streamwise wavelength of the free-stream disturbance and $\lambda_{x,\mathrm{bl}}$ is the streamwise wavelength of the boundary-layer perturbation $\acute{\mathbf{q}}$ sufficiently downstream from the leading edge.

sufficiently upstream and away from the plate, have the form

$$\mathbf{u} - \mathbf{i} = \epsilon \hat{\mathbf{u}}^\infty \, e^{i\left(\mathbf{k}\cdot\mathbf{x} - k_x \mathtt{R}\hat{t}\right)} + \text{c.c.}, \tag{1}$$

where c.c. indicates the complex conjugate, ϵ is a small parameter, $\mathbf{i}$ is the unit vector along the streamwise direction, and $\hat{t}$ is the dimensionless time defined below. The wavenumber vector $\mathbf{k} = \{k_x, k_y, k_z\}$ and the amplitude of the free-stream velocity disturbance $\hat{\mathbf{u}}^\infty = \{\hat{u}^\infty, \hat{v}^\infty, \hat{w}^\infty\}$ satisfy the solenoidal condition $\mathbf{k} \cdot \hat{\mathbf{u}}^\infty = 0$. Lengths are scaled by $\Lambda_z^* = \lambda_z^*/2\pi$, where λ_z^* is the spanwise wavelength of the gust. As the flow is periodic along the spanwise direction and the boundary-layer dynamics is linear because the perturbation is assumed of small amplitude, λ_z^* is also the spanwise wavelength of the Görtler vortices. Velocities are scaled by U_∞^*, the temperature is scaled by T_∞^*, and the pressure is scaled by $\rho_\infty^* U_\infty^{*2}$, where ρ_∞^* is the mean density of air in the free stream.

The Reynolds number is defined as $\mathtt{R} = U_\infty^* \Lambda_z^*/\nu_\infty^* \gg 1$, where ν_∞^* is the kinematic viscosity of air in the free stream, the Görtler number is $\mathtt{G} = \mathtt{R}^2 \Lambda_z^*/r^* = \mathcal{O}(1)$, and the Mach number is defined as $\mathtt{M} = U_\infty^*/a_\infty^* = \mathcal{O}(1)$, where $a_\infty^* = (\gamma \mathcal{R}^* T_\infty^*)^{1/2}$ is the speed of sound in the free stream, $\mathcal{R}^* = 287.06$ J kg^{-1} K^{-1} is the ideal gas constant for air, and $\gamma = 1.4$ is the ratio of specific heats. The dimensionless spanwise wavenumber is $k_z = 1$ and the frequency parameter is $k_x \mathtt{R} = 2\pi \Lambda_z^{*2} U_\infty^*/(\lambda_x^* \nu_\infty^*)$. The streamwise coordinate and time are scaled as $\hat{x} = x^*/(\mathtt{R}\Lambda_z^*)$ and $\hat{t} = U_\infty^* t^*/(\mathtt{R}\Lambda_z^*)$, respectively, due to our interest in streamwise elongated perturbations.

We restrict ourselves to cases for which the highly-oblique Tollmein-Schlichting waves investigated by Ricco and Wu (2007) do not occur.

3.1   Flow decomposition

The boundary-layer velocity, pressure, and temperature $\mathbf{q} = \{u, v, w, p, \tau\}$ are decomposed into their mean $\mathbf{Q}$ and perturbation $\acute{\mathbf{q}}$ as $\mathbf{q}(\mathbf{x}, t) = \mathbf{Q}(\mathbf{x}) + \epsilon \, \acute{\mathbf{q}}(\mathbf{x}, t)$. Under the assumption $r \gg 1$, curvature effects on the mean flow can be neglected (Spall and Malik, 1989). Consequently, at leading order the mean flow behaves as if the plate were flat. The Dorodnitsyn-Howarth transformation can then be applied to obtain the mean-flow momentum equation $\mathcal{M}$ and energy equation $\mathcal{E}$ in similarity form (Stewartson, 1964) introducing the compressible Blasius function $F = F(\eta)$, the temperature $T = T(\eta)$, and the dynamic viscosity $\mu(T) = T^\omega$, where $\omega = 0.76$ (Stewartson, 1964). The independent similarity variable is defined as $\eta = \bar{Y}/(2\hat{x})^{1/2}$, where $\bar{Y}(\hat{x}, y) = \int_0^y 1/T(\hat{x}, \bar{y})\mathrm{d}\bar{y}$

3

and the Prandtl number, assumed to be constant, is $\mathtt{Pr} = 0.707$. The streamwise velocity U and the wall-normal velocity V of the mean flow are

$$U = F', \qquad V = \frac{T(\eta_c F' - F)}{\mathtt{R}(2\hat{x})^{1/2}}, \tag{2}$$

where $\eta_c(\eta) = T^{-1} \int_0^\eta T(\hat{\eta}) \mathrm{d}\hat{\eta}$ (Stewartson, 1964).

3.2 The compressible boundary-region equations with curvature effects

The theoretical framework used herein is a combination of the work of Wu et al. (2011) on incompressible Görtler flows over concave surfaces with the work of Ricco and Wu (2007) on compressible Klebanoff modes over flat surfaces. Both papers are extensions of the original theory developed by Leib et al. (1999) for the incompressible flat-plate case.

The boundary-layer perturbations are assumed to be periodic in time t and along the spanwise direction z. They are expressed as in Gulyaev et al. (1989),

$$\acute{\mathbf{q}}(\mathbf{x}, t) = ik_z \breve{w} \left\{ \mathtt{R}\bar{u}, \ (2\hat{x})^{1/2}\bar{v}, \ \frac{1}{ik_z}\bar{w}, \ \frac{1}{\mathtt{R}}\bar{p}, \ \mathtt{R}\bar{\tau} \right\} e^{i(k_z z - k_x \mathtt{R}\hat{t})} + \text{c.c.}, \tag{3}$$

where $\breve{w} \equiv \hat{w}^\infty + ik_z \hat{v}^\infty (k_x^2 + k_z^2)^{-1/2}$ and $\bar{\mathbf{q}}(\hat{x}, \eta) = \{\bar{u}, \bar{v}, \bar{w}, \bar{p}, \bar{\tau}\}(\hat{x}, \eta)$. Starting from the full compressible Navier-Stokes and continuity equations in curvilinear coordinate form, using the Lamé coefficients and the scaling previously introduce we find the perturbation equations in which (2) and (3) are substituted. Then, taking the limits $\mathtt{R} \to \infty$ and $k_x \to 0$ with $k_x \mathtt{R} = \mathcal{O}(1)$, the LUBR equations with the appropriate initial and boundary conditions are obtained (Viaro and Ricco, 2018b). Gulyaev et al. (1989), Choudhari (1996), and Leib et al. (1999) recognized that the LUBR equations, complemented by rigorous initial and free-stream boundary conditions, must be used to study the flow in region III and II of figure 1.

3.3 The eigenvalue equations with curvature effects

Because of the inviscid unbalance between the centrifugal force and the wall-normal pressure, the Görtler instability exhibits an exponential streamwise amplification. Following the work of Wu et al. (2011), we can take advantage of this property by adopting a simplified mathematical framework based on an additional decomposition of the quantities defined in (3),

$$\bar{\mathbf{q}}(\hat{x}, \eta) = \{\bar{u}, \bar{v}, \bar{w}, \bar{p}, \bar{\tau}\} \equiv \widetilde{\mathbf{q}}(\eta) \, e^{\int^{\hat{x}} \sigma_{\text{EV}}(x) \mathrm{d}x}, \tag{4}$$

where $\widetilde{\mathbf{q}} = \{\widetilde{u}, \widetilde{v}, \widetilde{w}, \widetilde{p}, \widetilde{\tau}\}$ and $\sigma_{\text{EV}} = \sigma_{\text{EV, Re}} + i\sigma_{\text{EV, Im}}$ is a complex function whose real part $\sigma_{\text{EV, Re}}(\hat{x})$ is the local growth rate and the imaginary part $\sigma_{\text{EV, Im}}(\hat{x})$ is proportional to the streamwise wavenumber of the boundary-layer perturbation, i.e., $k_{x, \text{EV}}(\hat{x}) = \frac{1}{\hat{x}} \int^{\hat{x}} \sigma_{\text{EV}}(x) \mathrm{d}x$. Expression (4) is a local eigenvalue (EV) decomposition, i.e., valid at a specified streamwise location, which implies that the streamwise dependence of the perturbation is absorbed in $\sigma(\hat{x})$, while the wall-normal variation is distilled in $\widetilde{\mathbf{q}}(\eta)$. The EV perturbation (4) is only defined within an undetermined amplitude which can only be found through the receptivity analysis, i.e., by accounting for the influence of the free-stream disturbance. Nevertheless, upon comparison with the LUBR solution, the EV approach identifies the streamwise locations where the perturbation exhibits exponential growth and where its growth rate and streamwise length scale are not influenced by the initial and free-stream boundary conditions.

By substituting (4) into the LUBR equations we obtain the non-parallel EV system of equations, which preserves the growing nature of the boundary-layer mean flow. The equations can be further simplified by invoking the η-based parallel mean-flow assumption, which implies $V = 0$, and by taking the limit $\hat{x} \gg 1$ (Wu et al., 2011). The non-parallel compressible EV equations are given in Viaro and Ricco (2018b).

3.4 Asymptotic analysis

We herein extend the asymptotic analysis of Wu et al. (2011) for $G \to \infty$ to the compressible case with $M = \mathcal{O}(1)$. A summary of the physical results extracted through the asymptotic analysis of this section is given in §3.4.1, while the complete theoretical derivation can be found in Viaro and Ricco (2018b). Even though this theoretical analysis unveils crucial physical characteristics which are not revealed by a purely numerical approach, it will become evident that the numerical solution of the LUBR equations is nevertheless needed for a thorough understanding of the flow and for its accurate computation, especially for $G = \mathcal{O}(1)$, where the asymptotic analysis is invalid.

3.4.1 Physical summary

From the asymptotic analysis in the limit of large Görtler number, we can infer the following physical properties:

- as in the incompressible case, the unbalance between pressure and centrifugal forces triggers the Görtler instability at a streamwise location $\hat{x} = \mathcal{O}\left(G^{-2/5}\right)$, i.e., when both the wall-normal and the spanwise pressure gradients are active in the wall-normal and spanwise momentum equations, respectively;

- in stage II, i.e., where the boundary-layer equations describe the flow as the spanwise viscous diffusion effects are negligible, increasing the Mach number causes:

    - the boundary-layer perturbation to intensify;
    - the perturbation to shift away from the wall;

- in stage III, i.e., further downstream where the flow is described by the boundary-region equations because the spanwise viscous diffusion and the spanwise pressure gradient are at work:

    - the growth rate decreases slightly downstream;
    - increasing the Mach number has a stabilizing effect on the growth rate, which is more intense in supersonic flow conditions ;
    - for $M = \mathcal{O}(1)$, the vortices move towards the wall as the Mach number increases;
    - we have obtained a composite asymptotic solution, whose near-wall part is fully viscous and adiabatic, while the part in the boundary-layer core is inviscid.

3.5 Neutral curve parameters

The neutral curves are represented in the $\hat{x}$-G plane by the parameters (Viaro and Ricco, 2018a)

$$\varsigma(\hat{x}) \equiv \frac{\mathrm{d}E(\hat{x})}{\mathrm{d}\hat{x}}, \qquad\qquad \beta(\hat{x}) \equiv \frac{\mathrm{d}^2|\bar{u}(\hat{x})|_{\mathrm{max}}}{\mathrm{d}\hat{x}^2}, \tag{5}$$

where $E(\hat{x}) \equiv \int_0^\infty |\bar{u}(\hat{x}, \eta)|^2 \mathrm{d}\eta$ is the scaled perturbation energy divided by $(2\hat{x})^{1/2}$ (Hall, 1990) and $|\bar{u}(\hat{x})|_{\mathrm{max}} \equiv \max_\eta |\bar{u}(\hat{x}, \eta)|$ is the maximum along $\eta = y/(2\hat{x})^{1/2}$ of the amplitude of the streamwise velocity perturbation. This definition of $\varsigma(\hat{x})$ is well suited for the receptivity analysis since it retains the information from the perturbation amplitude. The latter would not enter the picture if the $\hat{x}$-derivative of the energy were normalized by the energy itself, as in Hall (1990). Only the $|\bar{u}|$ component is used to define the scaled perturbation energy in (5) because the physical streamwise velocity component for the Görtler vortices is much larger than the transverse velocity components (Wu et al., 2011).

The flow is unstable for $\varsigma > 0$ and stable for $\varsigma < 0$, with $\varsigma = 0$ defining the neutral points located at $\hat{x} = \hat{x}_{\varsigma_0}$. Since curvature effects are not at work near the leading edge, the boundary-layer

perturbations start growing from the leading edge as Klebanoff modes, herein labelled K-vortices Ⓚ, for which $\varsigma > 0$, $\beta < 0$. Depending on G, k_xR and k_y, K-vortices can either become stable downstream of $\hat{x} = \hat{x}_{\varsigma_0}$ or turn into Görtler vortices at $\hat{x} = \hat{x}_K$, where $\beta = 0$ and $\beta'(\hat{x}) > 0$, with the prime indicating the derivative with respect to $\hat{x}$. The Görtler vortices are characterized by an initial strong growth, denoted by Ⓖₛ, for which $\beta > 0$ (Gₛ-vortices). When $\beta = 0$ and $\beta' < 0$ at $\hat{x} = \hat{x}_G$, the local growth rate is maximum and downstream their growth weakens as $\beta < 0$ (Gw-vortices, Ⓖw), until they eventually stabilize downstream of $\hat{x} = \hat{x}_{\varsigma_0}$.

4   Numerical results

4.1   Unsteady boundary-region results

Using the LUBR equations, we investigate the dependence of the evolution of compressible Görtler vortices on four main parameters, i.e., the Mach number, the Görtler number, the ratio of the disturbance wavelengths in the free stream, and the frequency. In order to obtain realistic results, this parametric analysis is based on wind tunnel data of compressible flows.

4.1.1   Effect of Mach number

The effect of the Mach number is investigated while keeping a constant unit Reynolds number $R_u^* = U_\infty^*/\nu_\infty^*$. We consider the cases of steady vortices ($f^* = 0$) in conditions similar to the experimental configuration of De Luca et al. (1993), i.e., with spanwise wavelength $\lambda_z^* = 8 \cdot 10^{-3}$m, corresponding to R = 1273.2, and radius of curvature $r^* = 10$m, corresponding to G = 206.4. The Mach number is limited to M ≤ 4 to maintain valid the assumptions of ideal gas and constant Prandtl number. The dimensionless wall-normal coordinate $y_{99} \equiv y^*/\delta_{99}^*$ is used when comparing results at different Mach numbers.

We find that, for $\hat{x} = \mathcal{O}(1)$, increasing M decreases the growth rate, i.e., the kinematic Görtler vortices (Gᵥ-vortices) become more stable, especially for supersonic flows. This confirms the asymptotic results for stage III and is true only sufficiently downstream from the leading edge where the Görtler instability is fully developed and δ^* is comparable with λ_z^*. In the early stages of the streamwise-velocity perturbation where instead the spanwise viscous diffusion is negligible, the effect of the Mach number is reversed (not shown). This also confirms the theoretical results for stage II. The stabilizing effect of the Mach number when $\delta^* = \mathcal{O}(\lambda_z^*)$ is in accordance with early studies utilizing linearized theories for the primary instability (El-Hady and Verma, 1983; Spall and Malik, 1989). The most unstable Görtler vortices are therefore incompressible. However, this is true only during the initial stages of the evolution as the recent experimental study by Wang et al. (2018) showed that transition to turbulence is achieved more rapidly for compressible Görtler vortices compared to the slower transition of incompressible Görtler vortices because the secondary instability of nonlinearly evolving vortices is more intense in the compressible case.

In addition to Gᵥ-vortices, compressibility effects generate thermal Görtler vortices, hereinafter called Gₜ-vortices. They originate due to the velocity-temperature coupling within the boundary layer even in the absence of free-stream temperature disturbances, similar to the thermal Klebanoff modes over a flat plate (Ricco and Wu, 2007). Figure 2 (left) reveals that the temperature perturbations also grow exponentially and are more stable sufficiently downstream, i.e., their growth rate decreases, as the Mach number increases. However, thanks to our receptivity framework we notice that in the proximity of the leading edge, where δ^* is smaller than λ_z^*, the temperature perturbations increase much more significantly with the Mach number than the velocity perturbations. We further note that the stabilizing effect of the Mach number occurs much further upstream for the Gᵥ-vortices than for the Gₜ-vortices. Since further downstream the growth rate decreases with increasing M, temperature perturbations for lower M become dominant when $\hat{x}$ is sufficiently high. This reversed influence of compressibility caused by the growing presence of spanwise viscous
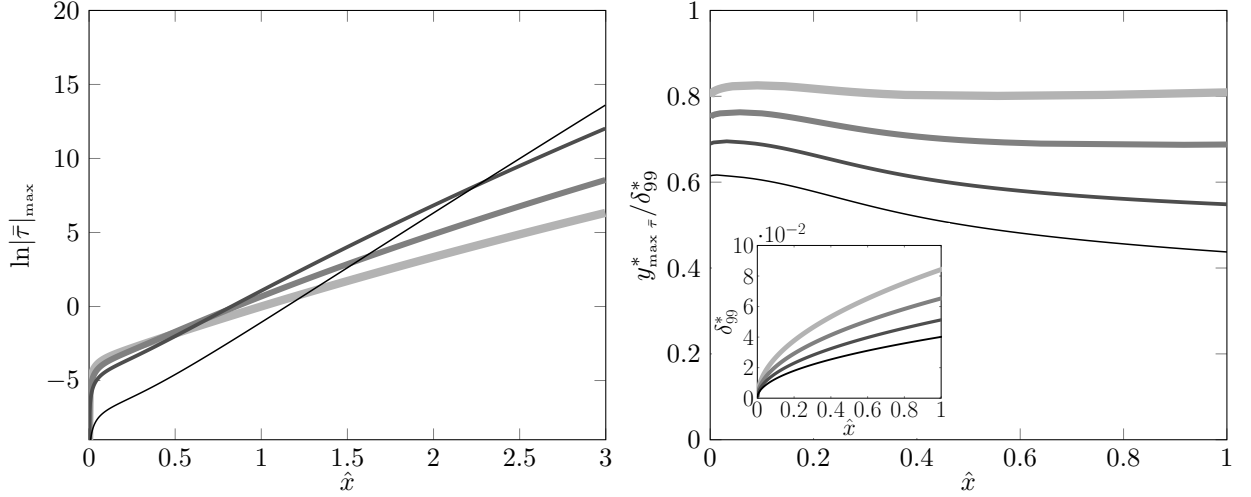
Figure 2: The effect of the Mach number on the maximum temperature perturbation (left) on the wall-normal location of G_T-vortices (right) for a steady flow at $R = 1273.2$, $G = 206.4$ and $k_y = 1$. Inset: Boundary-layer thickness based on $\lambda_z^* = 8 \cdot 10^{-3}$m, expressed in meters.

diffusion along the streamwise direction was also detected on thermal Klebanoff in the presence of wall heat transfer (Ricco et al., 2009).

The location of the maximum value of the perturbation amplitude is monitored to identify the wall-normal position of the Görtler vortices. Early studies by El-Hady and Verma (1983), and Ren and Fu (2015) show that the vortices lift away from the wall as the Mach number increases, although through EV approaches they could not trace the evolution of the vortices from the leading edge because the external forcing due to the free-stream disturbances plays a crucial role there. This effect of compressibility on Görtler vortices was also noticed by Spall and Malik (1989) and Hall and Fu (1989). Previous studies have shown that in the limit of large Mach number the vortices move into a log-layer near the free stream. However, as we focus on $M = \mathcal{O}(1)$, this lifting effect of the Mach number is not intense enough and the vortices are only confined in the core of the boundary layer. Thanks to our receptivity framework, we can follow the wall-normal location of G_V-vortices and G_T-vortices as they evolve from the leading edge. Figure 2 (right) confirms that by increasing the Mach number the G_T-vortices occur at larger wall-normal locations, also true for the G_V-vortices (not shown). The effect of M is stronger on the G_V-vortices than on the G_T-vortices and the G_T-vortices are positioned closer to the free stream than the G_V-vortices. The increase of boundary-layer thickness δ_{99}^* with M is also shown in the inset of figure 2 (right).

As shown by Hall (1983) and Wu et al. (2011), incompressible Görtler vortices move closer to the surface as they evolve downstream and they become confined in the wall layer region. This behavior persists even for compressible flows as long as $M < 3$. For $M \geq 3$ the vortices are not confined near the wall but they evolve in the core of the boundary layer. The asymptotic results of stage III, which are based on the assumption $G \gg 1$, cannot capture this behavior because vortices tend to shift towards the wall as G increases for any Mach number when $M = \mathcal{O}(1)$.

4.1.2 Effect of Görtler number

In the context of steady vortices, we now analyze the effect of the Görtler number on the evolution of perturbations for $M = 2$ and $M = 4$. Keeping $R = 1273.2$, radii of curvature $r^* = 5$m and $r^* = 10$m give $G = 412.8$ and $G = 206.4$, respectively.

The evolution of the perturbation is characterized by the parameter $\beta(\hat{x}) \equiv d^2|\bar{u}(\hat{x})|_{\max}/d\hat{x}^2$ (Viaro and Ricco, 2018a). Klebanoff modes, for which $\beta < 0$ due to their algebraic growth, first develop near the leading edge. When curvature effects become important the perturbation shifts
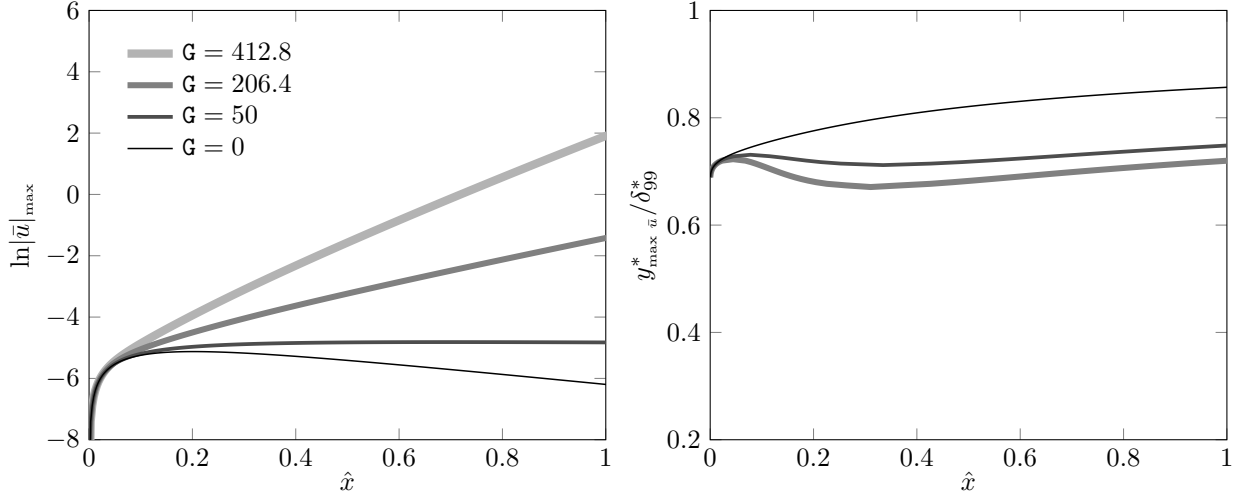
7

Figure 3: The effect of the Görtler number $\mathtt{G}$ on the maximum streamwise velocity perturbation (left) and on the wall-normal location of $\mathtt{G_V}$-vortices at $\mathtt{M} = 4$ (right) for a steady flow $\mathtt{R} = 1273.2$ and $k_y = 1$.

to Görtler vortices at a streamwise location $\hat{x}_\beta$ where $\beta = 0$ and starts growing with $\beta > 0$. The location $\hat{x}_\beta$ decreases as $\mathtt{G}$ increases for all $\mathtt{M}$ and for subsonic conditions there is no Mach number influence. For supersonic conditions and low enough $\mathtt{G}$, $\hat{x}_\beta$ increases with $\mathtt{M}$, but $\hat{x}_\beta$ becomes independent on $\mathtt{M}$ in supersonic conditions if $\mathtt{G}$ is sufficiently large.

Klebanoff modes contribute to the initial growth of the perturbation and, for sufficiently small Görtler numbers, i.e., $\mathtt{G} < 50$ for $\mathtt{M} = 4$, they stabilize after a certain streamwise location, as shown in figure 3 (left). Only when $\mathtt{G}$ is large enough the instability is characterized by the more energetic Görtler vortices. This is confirmed by the recent experimental study of Wang et al. (2018) where for low $\mathtt{G}$ values only weak streaky structures are present but when $\mathtt{G}$ increases the Görtler instability generates stronger vortices. We also noticed that $\mathtt{G_T}$-vortices are more unstable than $\mathtt{G_V}$-vortices at $\mathtt{M} = 4$ (not shown).

The location of $\mathtt{G_V}$-vortices is shown in figure 3 (right) for $\mathtt{M} = 4$. When $\mathtt{G}$ increases the vortices move closer to the wall whereas when $\mathtt{M}$ increases they move away from the wall. High Mach number flows tend to behave more similarly to the flat-plate scenario.

The influence of the Mach number changes as the Görtler number increases. The asymptotic analysis reveals that for $\mathtt{G} \gg 1$ an increase of $\mathtt{M}$ makes the vortices move towards the wall. This was also noticed by Dando and Seddougui (1993) and it is confirmed by the LUBR results for high $\mathtt{G}$. When $\hat{x}$ is held fixed and $\mathtt{M}$ is subsonic or mildly supersonic and increases, the vortices shift towards the boundary-layer core only when $\mathtt{G} = \mathcal{O}(1)$. In addition, the position of the vortices as $\hat{x} = \mathcal{O}(1)$ increases is affected by the Mach number being smaller or larger than 3 for $\mathtt{G} = \mathcal{O}(1)$.

4.1.3 Effect of the free-stream wavelength ratio

The effect of the free-stream wavelength ratio $k_y = \lambda_z^*/\lambda_y^*$ can only be studied through the receptivity formalism because k_y only appears in the initial and free-stream boundary conditions. Figure 4 shows the effect of k_y on the streamwise perturbation velocity (left) and the wall-normal location of $\mathtt{G_V}$-vortices (right) for $\mathtt{M} = 4$ and $\mathtt{G} = 206.4$. The weak effect of k_y increases at higher Mach numbers (not shown). The flow becomes slightly more stable as k_y increases, with the most unstable configuration achieved for $k_y = 0$. The growth rate of the streamwise velocity becomes nearly constant for sufficiently high $\hat{x}$. When the flow is more stable as k_y increases, the vortices initially tend to shift towards the wall but their wall-normal position becomes independent on k_y at sufficiently high values of $\hat{x}$, as shown in figure 4 (right). Contrary to the effect of Mach number
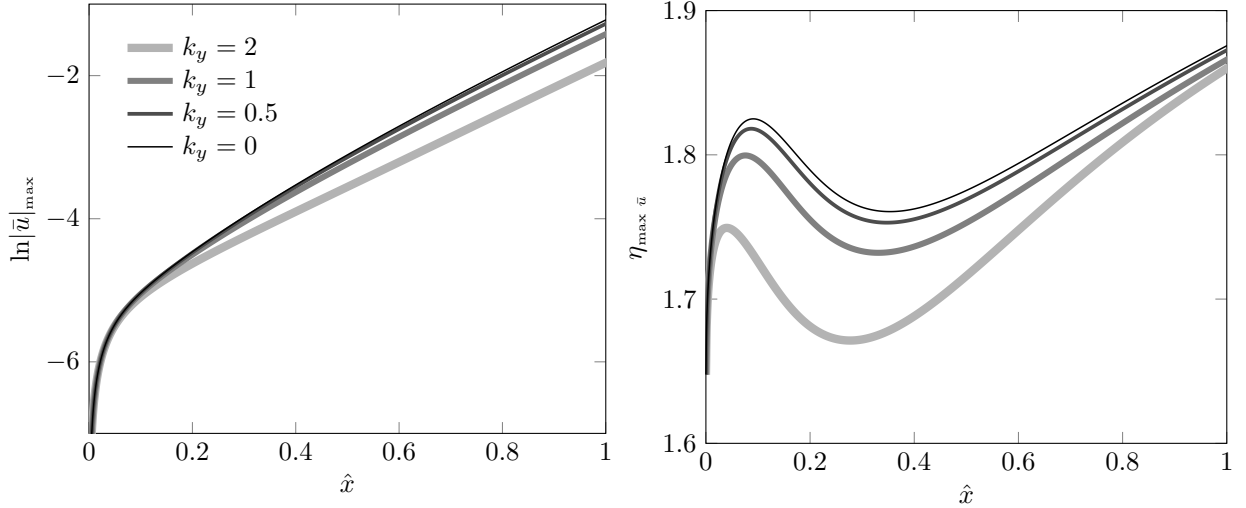
8

Figure 4: The effect of k_y on the maximum streamwise velocity perturbation (left) and wall-normal location of $\mathtt{G_V}$-vortices (right) for a steady flow at $\mathtt{R} = 1273.2$, $\mathtt{G} = 206.4$ and $\mathtt{M} = 4$.

and Görtler number, the influence of k_y on the wall-normal position of the vortices decreases as the streamwise location increases. Spall and Malik (1989) also noted that, for different initial conditions, the growth rates converged at sufficiently high scaled wavenumbers, i.e., sufficiently downstream, and that this convergence occurs closer to the leading edge as $\mathtt{G}$ increased. The normalized streamwise velocity and the temperature profiles experience no significant variations as k_y changes whereas the profiles of the crossflow velocities vary with k_y but only at small streamwise locations (not shown).

4.1.4 Effect of frequency

The effect of frequency at two different Mach numbers, $\mathtt{M} = 0.5$ and $\mathtt{M} = 3$, is investigated by keeping a constant dimensionless wavenumber $\kappa = k_z/(k_x \mathtt{R})^{1/2} = \mathcal{O}(1)$ which, for $\hat{x} = \mathcal{O}(1)$, is representative of the ratio $\delta^*/\lambda_z^* = \mathcal{O}(1)$, i.e., the spanwise and the wall-normal diffusion effects are comparable. Flows at different Görtler numbers are also compared for $r^* = 5$m and $r^* = 10$m. For the subsonic case the Görtler numbers are $\mathtt{G} = 2494.7$ and $\mathtt{G} = 1247.3$, whereas, for the supersonic case, $\mathtt{G} = 479.4$ and $\mathtt{G} = 239.7$, respectively. The frequency is scaled as $\mathtt{F} \equiv \frac{f^*}{\mathtt{R}_u^* U_\infty^*}$, where the unit Reynolds numbers are $\mathtt{R}_u^* = 11 \cdot 10^6$ m^{-1} and $\mathtt{R}_u^* = 2.18 \cdot 10^6$ m^{-1} for a subsonic case (Flechner et al., 1976) and a supersonic case (Graziosi and Brown, 2002), respectively. For each Mach number, the effect of frequency is studied by doubling and halving a reference frequency from wind tunnel experiments for supersonic and subsonic flows. At $\mathtt{M} = 3$, the reference frequency $f^* = 1000$Hz ($\mathtt{F} = 7.5 \cdot 10^{-7}$) comes from the work of Graziosi and Brown (2002), which corresponds to the maximum perturbation energy. Given that no experiments were found for $\mathtt{M} = 0.5$, the reference frequency $f^* = 250$Hz ($\mathtt{F} = 1.32 \cdot 10^{-7}$) was inferred from the knowledge of frequencies at very low Mach numbers (Boiko et al., 2010), $f_{\max}^* \approx 20$Hz, and at high Mach numbers (Graziosi and Brown, 2002), $f_{\max}^* \approx 10$kHz. This value additionally allows us to compare the same frequency, $f^* = 500$Hz, in the two Mach numbers considered.

Figure 5 (left) shows the stabilizing effect of increasing the frequency on the temperature perturbation while keeping a constant radius of curvature $r^* = 5$m. The stabilizing effect of doubling the reference frequencies is stronger compared to the destabilizing effect of halving them, for $\mathtt{M} = 3$ and for $\mathtt{M} = 0.5$, $r^* = 10$m (not shown). The same conclusions can be drawn for the maximum velocity perturbation $|\bar{u}(\hat{x})|_{\max}$, which also agree with the findings of Hall (1990) and Ren and Fu (2015). Frequency plays an important role on the location of Görtler vortices. As the main effect of increasing the frequency is to move the vortices away from the wall even for low
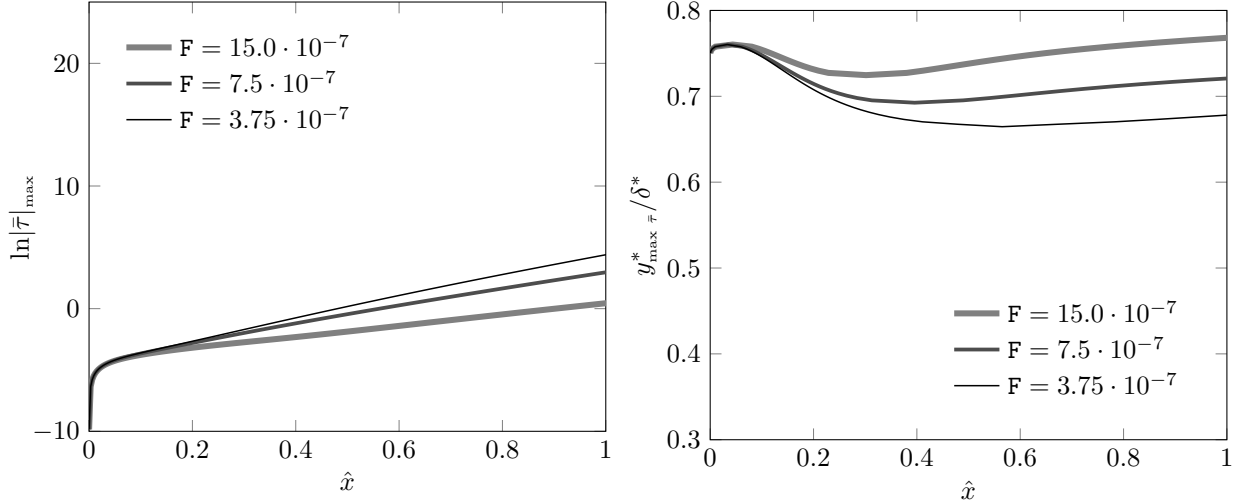
9

Figure 5: The effect of the frequency $\mathtt{F}$ on the maximum temperature perturbation (left) and on the wall-normal location of $\mathtt{G_T}$-vortices (right) for a plate with $r^* = 5\mathrm{m}$, $k_y = 1$, $\mathtt{G} = 479.4$ and $\mathtt{M} = 3$.

Mach numbers, e.g. $\mathtt{M} = 0.5$, $\mathtt{G_T}$-vortices are not confined near the wall if the frequency is high enough. At high Mach numbers, figure 5 (right) shows that the effect of frequency on the location of $\mathtt{G_T}$-vortices is more intense and starts closer to the leading edge. $\mathtt{G_V}$-vortices are located closer to the wall with a weaker dependence on the frequency than $\mathtt{G_T}$-vortices (not shown).

To summarize, Görtler vortices tend to move towards the boundary-layer core when the perturbation is more stable, i.e., as $\mathtt{F}$ or $\mathtt{M}$ increase, or $\mathtt{G}$ decreases. As k_y increases, the perturbation is slightly more stable and Görtler vortices tend to move closer to the wall.

4.2 Comparison with results from the eigenvalue analysis

Figure 6 shows the comparison between the growth rate (left) and the streamwise length scale ratio (right) of the LUBR solution and EV solution. The most important point is that the receptivity process selects the most unstable modes. The non-parallel EV solution (solid circles) is a better approximation for the growth rate and the streamwise length scale than the parallel EV solution (empty circles) at $\eta = 2$, where the growth rate is at its maximum. The non-parallel and parallel EV formulations show the strongest disagreement with the receptivity LUBR solution closer to the leading edge, where the solution has not yet acquired a modal form. In this region, the non-parallel effects, and the initial and free-stream boundary conditions thus play a key role in the dynamics of the perturbation. In the limit $\hat{x} \to 0$ the EV solution is invalid, with the growth rate becoming negative. Results show a tendency of the EV approach to overestimate the growth rate, which is in agreement with the results of Spall and Malik (1989). The agreement between the LUBR solution and the parallel EV solution is worse in the supersonic case than in the subsonic case. The use of the rigorous receptivity LUBR framework becomes therefore essential for supersonic flows.

4.3 Downstream evolution of the disturbance energy

The scaled perturbation energy $\mathtt{E}(\hat{x})$ of both $\mathtt{K}$-vortices and Görtler vortices, normalized by the maximum value $\mathtt{E}_{\max,\mathtt{G}_0} \equiv \max_{\hat{x}} |\mathtt{E}(\hat{x})||_{\mathtt{G}=0}$ for $\mathtt{G} = 0$, is shown in figure 7 (left) as a function of $\hat{x}$ for $k_x\mathtt{R} = 0$ and $k_y = 2$. Energy maxima, $\mathtt{M_1}$ and $\mathtt{M_2}$, and minima $\mathtt{m}$ identify stable conditions, i.e., where $\varsigma = 0$. Three critical Görtler numbers occur for this configuration, i.e., $\mathtt{G_A}$, $\mathtt{G_B}$, and $\mathtt{G_C}$. In the flat-plate case, for which $\mathtt{G} = \mathtt{G_A} = 0$, only $\mathtt{K}$-vortices are present. They start growing from the leading edge and then dissipate rapidly due to viscosity (Leib et al., 1999). As the curvature
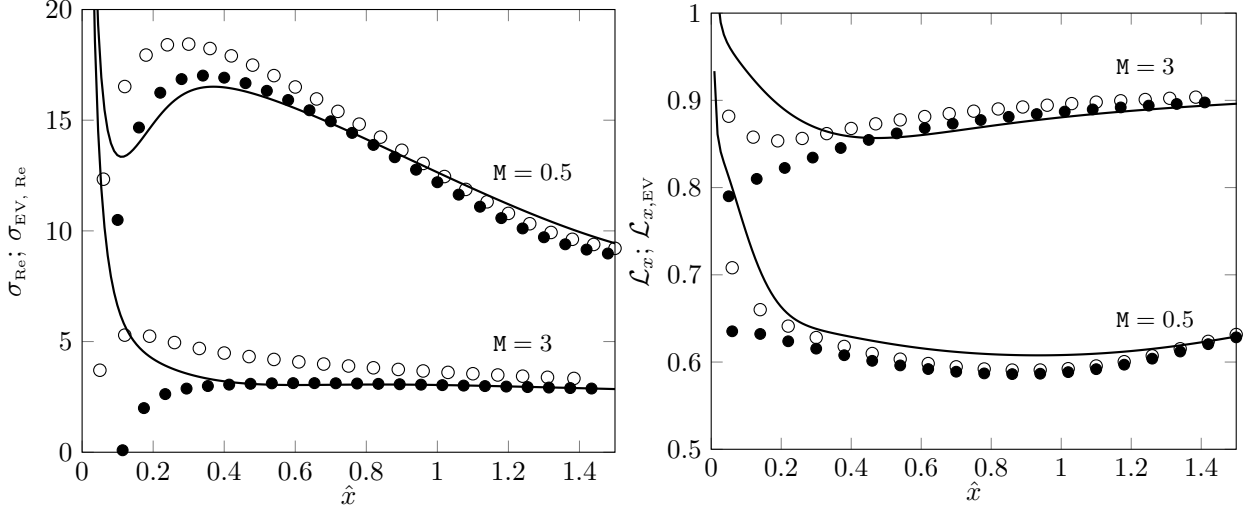
10

Figure 6: Comparison between the LUBR $\sigma_{\mathrm{Re}}(\hat{x}, \eta)$ (——) at $\eta = 2$, the non-parallel EV $\sigma_{\mathrm{EV,\,Re}}(\hat{x})$ (●), and the parallel EV $\sigma_{\mathrm{EV,\,Re}}(\hat{x})$ (○) (left) and comparison between the LUBR $\mathcal{L}_x(\hat{x}, \eta)$ (——) at $\eta = 2$, the non-parallel EV $\mathcal{L}_{x,\mathrm{EV}}(\hat{x})$ (●), and the parallel EV $\mathcal{L}_{x,\mathrm{EV}}(\hat{x})$ (○) (right), for $\mathtt{M} = 3$, $\mathtt{G} = 1247.3$, $k_y = 1$, $\mathtt{F} = 1.32 \cdot 10^{-7}$ and $\mathtt{M} = 3$, $\mathtt{G} = 239.7$, $k_y = 1$, $\mathtt{F} = 7.5 \cdot 10^{-7}$.
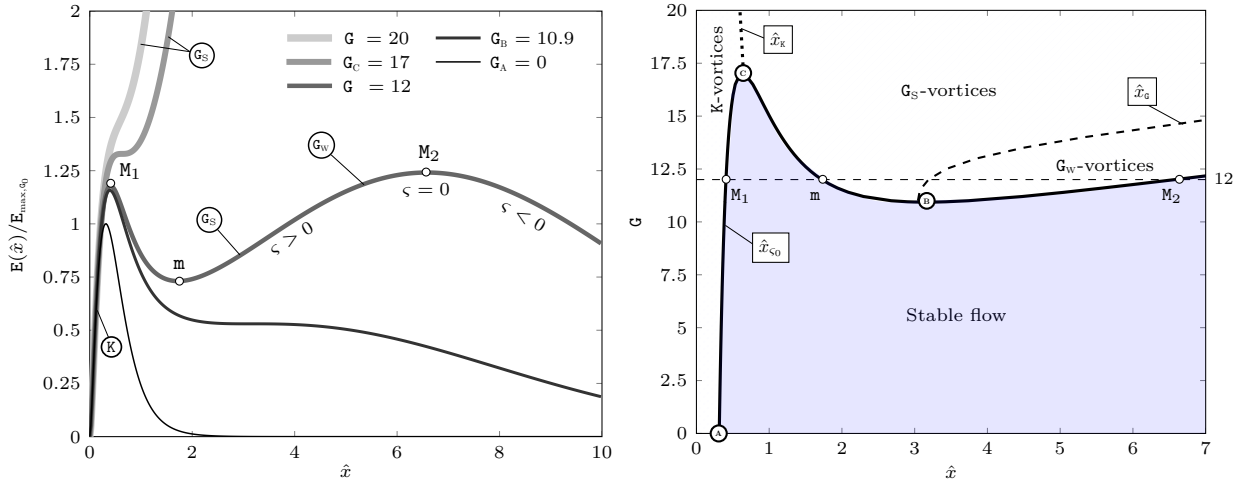
Figure 7: Perturbation energy $\mathtt{E}(\hat{x})$ normalized by $\mathtt{E}_{\max,\mathtt{G}_0}$, the maximum value of $\mathtt{E}$ for $\mathtt{G} = 0$, as a function of $\hat{x}$ (left) and neutral stability curve, $\hat{x} = \hat{x}_{\varsigma_0}$ (——), and curves at which the K-vortices turn into $\mathtt{G}_{\mathrm{S}}$-vortices, $\hat{x} = \hat{x}_{\mathtt{K}}$ (····), and the $\mathtt{G}_{\mathrm{S}}$-vortices turn into $\mathtt{G}_{\mathrm{W}}$-vortices, $\hat{x} = \hat{x}_{\mathtt{G}}$ (---) (right), for $k_x\mathtt{R} = 0$, $k_y = 2$.

11

is introduced, the imbalance between pressure and centrifugal forces energizes the boundary-layer perturbation. Only for $\mathtt{G} > \mathtt{G_B} = 10.9$ the Görtler vortices become unstable as secondary growing disturbances after the viscous decay of the K-vortices. A new maximum $\mathtt{M_2}$ thus emerges. Following the evolution of the perturbation for $\mathtt{G} = 12$, figure 7 (left) shows that K-vortices represent the initial instability of the boundary layer, which start stabilizing at $\mathtt{M_1}$. After the viscous decay, the onset of the Görtler vortices causes the boundary layer to become unstable again at $\mathtt{m}$. Their initial strong growth $\mathtt{\widehat{G_s}}$ shifts into a weak growth $\mathtt{\widehat{G_w}}$ at $\hat{x} = \hat{x}_\mathtt{G}$ before ultimately stabilizing again at $\mathtt{M_2}$. In the range $\mathtt{G_B} < \mathtt{G} < \mathtt{G_C} = 17$ both instabilities are thus present. Figure 7 (left) also shows that for $\mathtt{G} > \mathtt{G_C}$ the K-vortices turn into Görtler vortices directly without the intermediate viscous decay.

4.4 Neutral curves

4.4.1 Steady Görtler-flow scenario

The neutral curve for $k_x\mathtt{R} = 0$ and $k_y = 2$ is shown in figure 7 (right). The continuous black line represents the neutral curve, the black dotted line indicates the streamwise location $\hat{x}_\mathtt{K}$ where K-vortices turn into Görtler vortices directly, and the black dashed line represents the streamwise location $\hat{x}_\mathtt{G}$ where the growth of the Görtler vortices shifts from strong to weak. Three critical points of the neutral curve, A, B, C, are shown in figure 7 (right). Point A indicates the $\hat{x}$ location downstream of which the K-vortices are stable for $\mathtt{G} = 0$, while point B denotes the $\hat{x}$ location of the local minimum of the neutral curve, corresponding to the Görtler number ($\mathtt{G_B} = 10.9$) below which only K-vortices exist. Point C indicates the $\hat{x}$ location of the local maximum of the neutral curve corresponding to the Görtler number ($\mathtt{G_C} = 17$) above which K-vortices shift directly to Görtler vortices.

The neutral curve shows that K-vortices always exist near the leading edge for any Görtler number and that increasing the Görtler number strengthens the inviscid nature of the Görtler instability, thereby causing the unstable region to expand rapidly. As the curvature increases, the point $\mathtt{m}$, also shown in figure 7 (left), moves closer to the leading edge and eventually merges with $\mathtt{M_1}$ for $\mathtt{G} = \mathtt{G_C}$. For $\mathtt{G} > \mathtt{G_C}$, the boundary layer is unstable from the leading edge as K-vortices turn into Görtler vortices at $\hat{x} = \hat{x}_\mathtt{K}$. If the perturbation energy were defined by integrating $|\bar{u}|$ over y for the definition of ς, the neutral curve would be slightly shifted to lower $\mathtt{G}$ but would retain its shape.

4.4.2 Effect of frequency and wavelength ratio

Figures 8 show the influence of the frequency parameter $k_x\mathtt{R} = \mathtt{R}\lambda_z^*/\lambda_x^*$ (left) and the wavelength ratio $k_y = \lambda_z^*/\lambda_y^*$ (right) on the neutral stability curves. For all cases, the $\hat{x}_\mathtt{K}$ lines overlap for most Görtler numbers (not shown) and, sufficiently downstream, the neutral curves become independent of the initial conditions that are herein linked to the free-stream disturbances. Figure 8 (left) shows that the stability region expands significantly as the frequency increases for free-stream disturbances with equal transverse wavelengths λ_z^* and λ_y^* ($k_y = 1$). Boundary-layer perturbations generated by steady free-stream disturbances are therefore the most likely to turn into Görtler vortices through inviscid instability. When $k_x\mathtt{R} > 2$, there is a range of Görtler numbers for which the boundary layer becomes unstable again after an initial decay of Görtler vortices and before entering the permanent stable region. This scenario is shown in figure 8 (left) for $k_x\mathtt{R} = 6$ and $\mathtt{G} = 55$. For higher frequencies, this phenomenon is even more accentuated as it occurs for a larger range of Görtler numbers. However, we focus on low-frequency disturbances as these are the most unstable and are fully consistent with our asymptotic framework, which is based on $k_x \ll 1$.

The inset of figure 8 (left) shows the increase of the critical Görtler number $\mathtt{G_B}$ with $k_x\mathtt{R}$. Results for different k_y are not shown as they overlap on the same curve due to $\mathtt{G_B}$ being near the location where the neutral curves are independent of k_y.

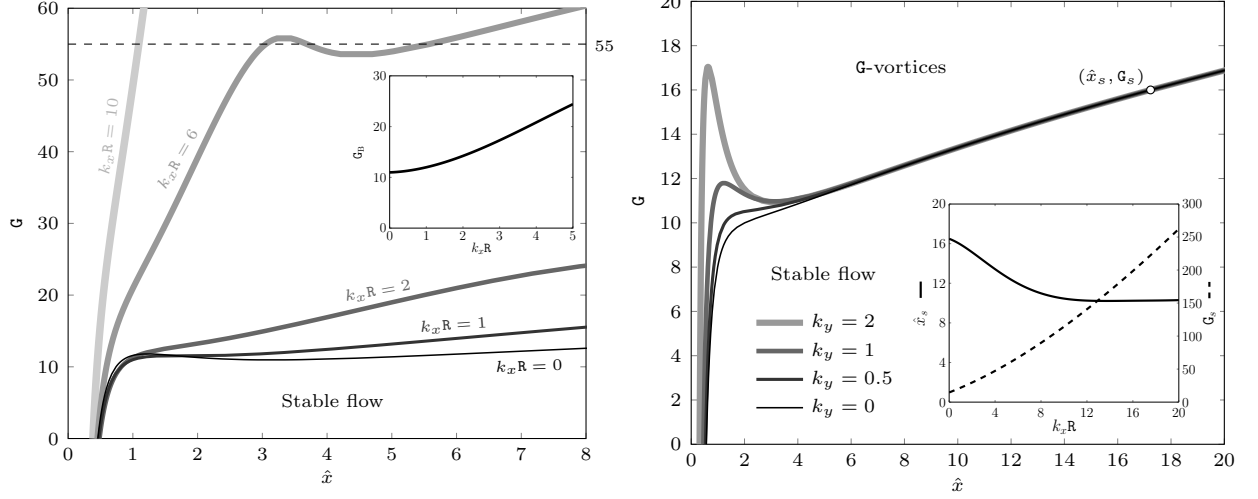Figure 8 (right) shows the influence of the wall-normal wavenumber k_y for $k_x\mathtt{R} = 0$. The most

12

Figure 8: Neutral stability curves $\varsigma = 0$ for $k_y = 1$ and different values of the frequency $k_x\mathtt{R}$. Inset: variation of the critical Görtler number $\mathtt{G_B}$ as a function of $k_x\mathtt{R}$ for $k_y = 1$ (left), and neutral stability curves for different values of the wall-normal wavenumber k_y and $k_x\mathtt{R} = 0$. Inset: streamwise location $\hat{x}_s$ where the neutral curve becomes independent on k_y and the corresponding Görtler number $\mathtt{G_s}$ for different frequencies $k_x\mathtt{R}$ (right).

critical scenario is for $k_y = 0$. As k_y increases, i.e., as λ_z^* becomes progressively larger than λ_y^*, stability increases near the leading edge for both steady and unsteady flows, whereas the neutral curve becomes independent of k_y downstream of a location $\hat{x}_s$, defined as the $\hat{x}$ location where the neutral points at different k_y remain within a range $\Delta\hat{x} < 0.0005$. This is in agreement with the results of Hall (1990) at large $\hat{x}$ locations. The streamwise location $\hat{x}_s$ is shown as a function of $k_x\mathtt{R}$ in the inset of figure 8 (right). As the frequency increases, $\hat{x}_s$ decreases and it becomes nearly independent of the frequency for $k_x\mathtt{R} > 10$. The Görtler number $\mathtt{G_s}$ associated with $\hat{x}_s$ increases monotonically with $k_x\mathtt{R}$. Based on the experimental conditions of Boiko et al. (2010), $\hat{x}_s = 10$ corresponds to $x^* \approx 22$m, which means that the independence of the neutral curves on k_y is not reached in realistic scenarios. As k_y only occurs in the free-stream boundary conditions at leading order, this further confirms the crucial importance of solving the receptivity problem, i.e., of precisely specifying the free-stream disturbance, for the correct description of the Görtler-flow dynamics.

DISTRIBUTION A: Approved for public release; distribution unlimited

References

A.V. Boiko, A.V. Ivanov, Y.S. Kachanov, and D.A. Mischenko. Steady and unsteady Görtler boundary-layer instability on concave wall. *Europ. J. Mech. B/Fluids*, 29(2):61–83, 2010.

M. Choudhari. Boundary layer receptivity to three-dimensional unsteady vortical disturbances in the free stream. *AIAA Paper 96-0181*, 1996.

A.H. Dando and S.O. Seddougui. The compressible Görtler problem in two-dimensional boundary layers. *IMA J. Appl. Math.*, 51(1):27–67, 1993.

L. De Luca, G. Cardone, D. Aymer de la Chevalerie, and A. Fonteneau. Görtler instability of a hypersonic boundary layer. *Exp. Fluids*, 16:10–16, 1993.

N.M. El-Hady and A.K. Verma. Growth of Görtler vortices in compressible boundary layers along curved surfaces. *J. Eng. Applied Sc.*, 2(3):213–238, 1983.

S.G. Flechner, P.F. Jacobs, and R.T. Whitcomb. A high subsonic speed wind tunnel investigation of winglets on a representative second-generation jet transport wing. *NASA TN D-8264*, 1976.

P. Graziosi and G.L. Brown. Experiments on stability and transition at Mach 3. *J. Fluid Mech.*, 472:83–124, 2002.

A.N. Gulyaev, V.E. Kozlov, V.R. Kuzenetsov, B.I. Mineev, and A.N. Sekundov. Interaction of a laminar boundary layer with external turbulence. *Fluid Dynamics. Translated from Izv, Akad. Navk. SSSR Mekh. Zhid. Gaza 6, vol. 5, pp. 55-65.*, 24(5):700–710, 1989.

P. Hall. The linear development of Görtler vortices in growing boundary layers. *J. Fluid Mech.*, 130:41–58, 1983.

P. Hall. Görtler vortices in growing boundary layers: the leading edge receptivity problem, linear growth and the nonlinear breakdown stage. *Mathematika*, 37(74):151–189, 1990.

P. Hall and Y. Fu. On the Görtler vortex instability mechanism at hypersonic speeds. *Theor. Comp. Fluid Dyn.*, 1(3):125–134, 1989.

S.J. Leib, D.W. Wundrow, and M.E. Goldstein. Effect of free-stream turbulence and other vortical disturbances on a laminar boundary layer. *J. Fluid Mech.*, 380:169–203, 1999.

J. Ren and S. Fu. Secondary instabilities of Görtler vortices in high-speed boundary layer flows. *J. Fluid Mech.*, 781:388–421, 2015.

P. Ricco and X. Wu. Response of a compressible laminar boundary layer to free-stream vortical disturbances. *J. Fluid Mech.*, 587:97–138, 2007.

P. Ricco, D.-L. Tran, and G. Ye. Wall heat transfer effects on Klebanoff modes and Tollmien-Schlichting waves in a compressible boundary layer. *Phys. Fluids*, 21(024106), 2009.

R.E. Spall and M.R. Malik. Görtler vortices in supersonic and hypersonic boundary layers. *Phys. Fluids*, 1(11):1822–1835, 1989.

K. Stewartson. *The theory of laminar boundary layers in compressible fluids*. Oxford, Claredon Press, 1964.

S. Viaro and P. Ricco. Neutral stability curves of low-frequency Görtler flow generated by free-stream vortical disturbances. *J. Fluid Mech.*, 845(R1), 2018a.

S. Viaro and P. Ricco. Compressible unsteady Görtler vortices subject to free-stream vortical disturbances. *J. Fluid Mech.*, JFM-18-S-1023.R1, 2018b.

Q.-C. Wang, Z.-G. Wang, and Y.-X. Zhao. Visualization of Görtler vortices in supersonic concave boundary layer. *J. Visual.*, 21(1):57–62, 2018.

X. Wu, D. Zhao, and J. Luo. Excitation of steady and unsteady Görtler vortices by free-stream vortical disturbances. *J. Fluid Mech.*, 682:66–100, 2011.